A fast bismuth-carbon composite anode for achieving kinetic matching between the anode and cathode of sodium-ion capacitors

Man Xiaoge[1], Huang Xinli[1,*], Min Xinyue[1], Yan Yijie[1], Shi Yuanchang[1,*], Li Tao[2,3], Wang Chengxiang[1], Zhang Zhiwei[1], Yin Longwei[1], Wang Rutao[1,2,*]

(1. *Key Laboratory for Liquid-Solid Structural Evolution and Processing of Materials*, *Ministry of Education*, *School of Materials Science and Engineering*, *Shandong University*, *Ji'nan* 250061, *China*;
2. *Key Laboratory of Advanced Energy Materials Chemistry (Ministry of Education)*, *Nankai University*, *Tianjin* 300071, *China*;
3. *Department of Materials Engineering*, *Xuzhou College of Industrial Technology*, *Xuzhou* 221140, *China*)

Abstract: Sodium-ion capacitors (SICs) typically feature a hybrid design, incorporating a battery-type anode that operates by faradaic redox reactions and an activated carbon cathode that functions through electrical double-layer (EDL) adsorption/desorption. However, the kinetics of faradaic processes are inherently slower than those of EDL processes, leading to a fundamental problem known as kinetic imbalance between the electrodes, which hinders the development of high-performance SICs. To address this, we synthesized composites of bismuth nanoparticles in N-doped carbon (Bi@NC) by a high-temperature sintering method. The resulting Bi@NC anode has a specific capacity of 300 mAh g^{-1} at 0.5 A g^{-1}, an exceptional rate capability (maintaining performance at currents exceeding 75 A g^{-1}), and outstanding cycling stability over 12 000 cycles. Three-electrode Swagelok cell tests revealed that this high-rate Bi@NC composite effectively decreases the kinetic gap with the activated carbon cathode, as shown by an analysis of their respective potential swing windows (vs. Na/Na^+). This enables the fabricated SIC to achieve a maximum energy density of 115 Wh kg^{-1}, a peak power density of 45 535 W kg^{-1}, and a long cycle life exceeding 8 000 cycles.

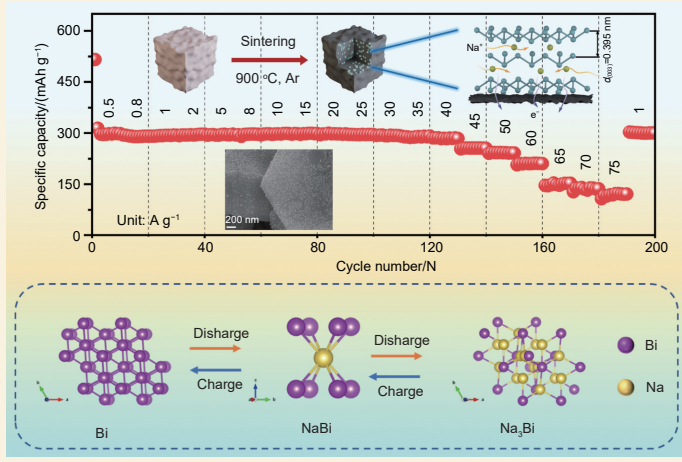

Key words: Bismuth anode; Carbon composites; Sodium-ion capacitors; Alloying anode; Sodium-ion storage

1 Introduction

Since Sony's commercialization of lithium-ion batteries, the fields of portable electronics and electric vehicles (EVs) have entered a period of significant advancement and growth[1]. Nevertheless, the elevated extraction costs associated with lithium ore, coupled with its adverse environmental impact, are incongruent with the principles of sustainable development[2–3]. Owing to the extensive crustal abundance and economy, sodium-ion capacitors (SICs) have become the attractive choice for the next-generation of energy storage technology[4–8]. As a category of metal ion capacitors, SICs comprise a battery-type anode and a capacitive cathode, thereby possessing the multiple characteristics of high energy and power densities[9–11]. Activated carbon (AC) is presently widely utilized as a cathode material of a capacitor with highly porous structure, economic viability, and excellent physicochemical properties[12–15]. Furthermore, the abundance of micropores and mesopores on the AC surface facilitates rapid mass transfer, thereby exhibit-

Received: October 09, 2025
Revised: December 18, 2025
Accepted: December 19, 2025

ing superior kinetic performance[16]. Among the diverse range of anode materials, carbon-based materials are the most extensively utilized[17–21]. However, the large ionic radius of Na^+ contributes to the sluggish reaction rate observed at the anode, which leads to poor rate capability[22]. Sluggish reaction kinetics of the anode may further reduce the capacity utilization of a capacitive cathode, which in turn affects the overall capacitor energy density[23]. Exploring and designing anodes with high-rate performance to accommodate the kinetic mismatch in SICs is of great importance.

Recently, alloy-based anode materials have been widely investigated due to the high reversible sodium storage capacity and high conductivity. Among them, bismuth has excellent properties such as low and suitable sodium storage potential and high theoretical specific capacity[24–29]. Moreover, it has been confirmed that the bismuth-sodium system has the highest conductivity and sodium diffusivity of all metal-sodium systems[30–31], showing kinetics that can be matched with the cathode material. This is because in the ether-based electrolyte, the bismuth metal can gradually undergo nanostructure evolution during the cycle to form a porous structure, providing a fast channel for Na^+ transport. Moreover, pioneering work has shown that unlike Pb, Sn and other metals, the alloy phase of Bi and Na is a 3D graphite phase with high electronic conductivity, rather than a high-resistance Zintl phase[32–33]. This endows the Bi anode material with kinetic characteristics comparable to AC. However, a significant volumetric expansion is unavoidable during the sodium storage process, resulting in anode pulverization, shielding of current collector and ultimately battery failure, which greatly limits the application of Bi-based anode materials. Solving this problem is of great significance for realizing SICs with cathode-anode kinetic matching.

Herein, we report a composite of N-doped carbon coating on bismuth metal nanoparticle (Bi@NC) prepared by a one-step sintering method. The Bi@NC anode material demonstrates superior overall electrochemical characteristics, encompassing a high theoretical capacity, exceptionally high rate, and prolonged cyclability. The high-rate characteristic of Bi@NC comes from its fast reaction kinetics, which can effectively realize the kinetic matching of a SIC. Furthermore, the SIC constructed using Bi@NC as the battery-type anode material demonstrates both elevated energy and power densities. In particular, this Bi@NC-based SIC yields a maximum energy density of 115 Wh kg^{-1}. Even at a high-power density of 45 535 W kg^{-1}, this SIC also sustains an energy density of 72 Wh kg^{-1}. These energy/power metrics surpass those reported for the majority of metal ion capacitors to date. Further, a three-electrode Swagelok cell (TESC) was used to dynamically detect the change in potential swing ranges of electrodes. The measurement results show that the cathode electrode voltage window increases slightly as the current density rises. This observation confirms that the enhanced kinetics of the anode electrode are compatible with the carbon cathode, which exhibits rapid kinetic behavior.

2 Experimental

2.1 Materials synthesis

Typically, 1.0 g commercial ammonium bismuth citrate ($C_6H_8BiNO_7$, 99%, Aladdin) was annealed at 900 °C for 1 h in argon atmosphere with a heating rate of 2 °C min^{-1}. The obtained black powder of bismuth nanoparticles@N-doped carbon (Bi@NC) was collected after cooling down to room temperature.

2.2 Characterization

Field emission scanning electron microscopy (FESEM, SU-70, Hitachi, Japan) and transmission electron microscopy (TEM, Tecnai F20, FEI Company, USA) were employed to investigate the morphologies and structural information of the samples. Powder X-ray diffraction (XRD, D/Max-2400, Rigaku, Tokyo, Japan) using Cu-*Kα* radiation was performed on samples to study the crystal structure and composition. Raman spectral analysis was performed on a JY-HR800 micro-Raman spectroscope with an excitation wavelength of 532 nm. The surface chemical species of as-prepared samples were recorded by an X-ray photoelectron spectroscopy (XPS,

AXIS Supra, UK). An ASAP 2020 volumetric adsorption analyzer (Micromeritics, USA) was used to probe the pore structures of as-prepared samples at 77 K.

2.3 Fabrication of half cells and hybrid cells

Typically, 80% of Bi@NC, 10% of acetylene black (conducting filler), and 10% of binder-polyvinylidene fluoride (PVDF) dissolved into methy l-2-pyrrolidone (NMP) were mixed in a mortar. The slurry was coated on the copper foil and dried at 80 °C under vacuum for 6 h. The foil was punched into a round electrode with a diameter of 14 mm. The mass loading of active materials was 1–2 mg. For cathode materials, a homemade polyaniline-derived porous carbon (PDPC) was used.

For half cells, the 2032 type-coin cell was assembled using Bi@NC as the working electrode, metal Na as the reference and counter electrode, and a glass-fiber membrane (Whatman, USA) as the separator. For the fabrication of the hybrid cells (Sodium ion capacitors, SICs), the Bi@NC anode was pre-sodiated for 3 cycles under 0.1 A g^{-1}, and ended in a sodium state at 0.01 V in a half cell. The pre-sodiated electrode was obtained by detaching the half cell in glovebox. The pre-sodiated Bi@NC anode coupled with PDPC cathode was assembled in the 2032-type coin-cell using the glass-fiber membrane (Whatman, USA) as the separator and 1 mol L^{-1} $NaPF_6$ in ethylene glycol dimethyl ether (DME) as the electrolyte. For all the cells, only ~ 80 μL of electrolyte was added. All cells were assembled in a glove box filled with highly pure argon (O_2 and H_2O levels < 0.1 ppm). When assembling three-electrode Swagelok cells (E200, Tianjin Aida Ltd, China), the whole assembly process is similar to full cell except that metal K was used as the reference electrode.

2.4 Electrochemical tests

The electrochemical tests such as cyclic voltammograms (CV), galvanostatic charge/discharge (GCD), electrochemical impedance spectroscopy (EIS) and Galvanostatic intermittent titration technique (GITT) were performed on half-cells and capacitors. CV and GCD tests were also performed in the three-electrode system. The above electrochemical tests were performed on the CHI760E instrument from Chenhua, Shanghai, China and the Biologic SP-200 instrument from France. The perturbation voltage applied in the EIS test is 5 mV and the frequency range is 100 000–0.01 Hz. In the GITT test, a pulse discharge/charge was performed at a current density of 0.1 A g^{-1} for a duration of 5 min, followed by a static relaxation of 25 min to fully relax it to a quasi-equilibrium potential. The diffusion rate of ions is calculated by Fick 's second law, as shown in Eq. (1).

$$D = \frac{4}{\pi \cdot \tau}\left(\frac{m_B \cdot V_m}{M_B \cdot S}\right)^2\left(\frac{\Delta E_s}{\Delta E_\tau}\right)^2 \quad (1)$$

where τ is the pulse time, m_B, M_B and V_m are the active mass, molar mass and molar volume of the test electrode, respectively. S is the area of the electrode surface. ΔE_S and ΔE_τ are the changes of steady-state voltage and total voltage, respectively, which can be obtained from the GITT curves.

The peak currents (i) and scan rates (v) derived from the CV tests adhere to a power-law relationship as expressed by the subsequent Eq. (2):

$$i = av^b \quad (2)$$

where a and b are adjustable parameters. The b value is used to evaluate the control step. A b value of 0.5 indicates a diffusion-controlled kinetics, typical of battery-like behavior, whereas a b value of 1.0 reflects a surface-controlled kinetics, indicative of capacitive behavior. Furthermore, the percentage contribution of capacitance at various scan rates can be ascertained from the CV data using the subsequent Eq. (3):

$$i(V) = k_1 v + k_2 v^{\frac{1}{2}} \quad (3)$$

where the current i is measured at a specific potential, and parameters k_1 and k_2 assess the contributions from surface (capacitive) effects and diffusion control, respectively, and v is the scan rate.

The energy density and power density of a capacitor can be calculated by the Eq. (4 and 5):

$$E = \frac{\int I \cdot V(t)\,dt}{3.6m} \quad (4)$$

$$P = \frac{3600E}{\Delta t} \quad (5)$$

where E (Wh kg^{-1}) represents the energy density, P (W kg^{-1}) represents the power density, m is the total mass of the cathode and anode active materials. I, V

and Δt are the discharge current, the voltage window and the discharge time, respectively.

3 Results and discussion

Bi@NC composites were prepared through heating ammonium bismuth citrate at 900 °C for 1 h in argon atmosphere (Fig. 1a). To investigate the effect of sintering temperature on the material's morphology and electrochemical properties, the precursors were sintered at 800 and 1000 °C as controls. During high-temperature sintering, the organic ligands in the bismuth salt are carbonized to form a carbon matrix framework, and as sintering proceeds, the metal ions inside are reduced to the metal Bi, where NH_4^+ acts as a nitrogen source to achieve doping during sintering. Previous studies have shown that the presence of nitrogen sources can catalyze the formation of bismuth monoatomic phase and ultimately promote the uniform dispersion of bismuth atoms[34]. The as-formed 3D conductive carbon framework contributes high electronic conductivity to the composite, which provides the possibility for ultrafast charge and discharge rate[35]. The surface morphology of Bi@NC composites was observed by SEM. The Bi@NC com-

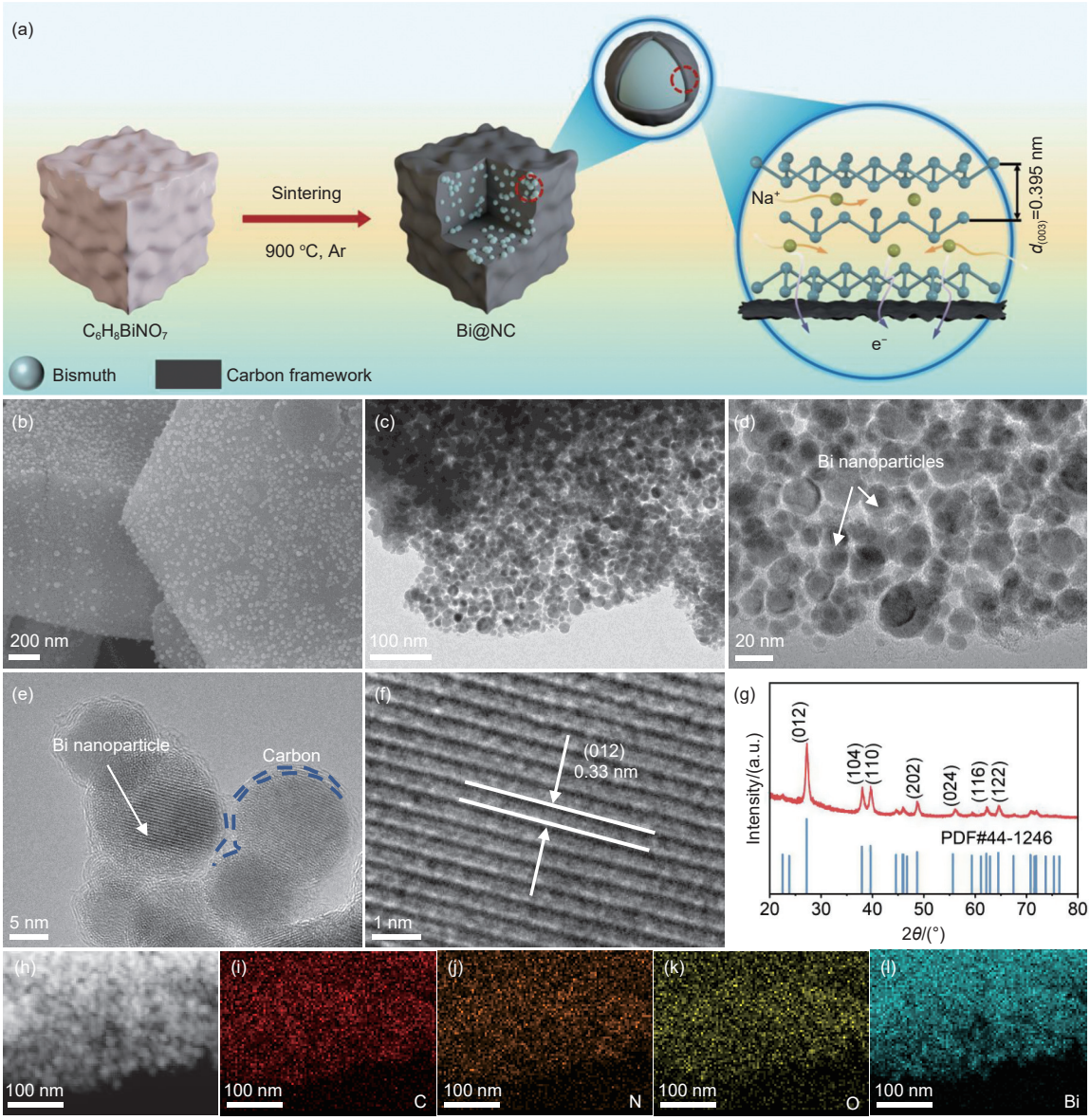

Fig. 1 The preparation method and structural characterization of Bi@NC. (a) Preparation schematic diagram of Bi@NC. (b)SEM and (c-f) TEM images. (g) XRD pattern. (h-l) Element mappings of C, N, O and Bi

posite exhibits regular bulk and the metal Bi particles with sizes of 10-20 nm are evenly distributed on the carbon matrix (Fig. 1b-e and Fig. S1). HRTEM was used to observe the binding of Bi nanoparticles to the inorganic carbon layer. The results show that the lattice of Bi nanoparticles is clearly visible and tightly wrapped by a uniform inorganic carbon layer (Fig. 1e). The ultrasmall Bi nanocrystals were verified by HRTEM in Fig. 1f and XRD pattern in Fig. 1g. HRTEM images show a lattice spacing of 0.33 nm corresponding to the Bi (012) crystallographic plane (PDF reference #44-1246). According to the Bragg equation, the interplanar spacing corresponds to the diffraction peak of the (012) crystal plane on the XRD pattern, and the sharp diffraction peak indicates that Bi in Bi@NC basically exists in the form of crystal. It is noted that the surface morphology and crystal structure of Bi@NC achieved at 800 and 1000 °C show no apparent different from Bi@NC achieved at 900 °C (Fig. S2 and S3). The selected-area electron diffraction (SAED) pattern exhibits a series of distinct and well-resolved diffraction rings, which further corroborates the high crystallinity of bismuth (Fig. S4). According to the position of the diffraction rings, these diffraction rings correspond to the (012), (104) and (110) crystal planes of the hexagonal phase Bi crystal. Well dispersion of Bi nanoparticles into N-doped carbon is confirmed by energy dispersive spectroscopy (EDS) mapping images (Fig. 1h-l and Fig. S5). Nitrogen adsorption-desorption isotherms of Bi@NC composites display a type IV adsorption-isotherm characteristics, indicating their mesoporous architecture. The specific surface area (SSA) of Bi@NC was measured to be 30.19 $m^2\ g^{-1}$, with the pore size predominantly centered around 9 nm (Fig. S6). Such mesoporous features facilitate rapid ion transport by providing efficient pathways, and the extensive specific surface area offers an increased number of reactive sites, thereby enhancing the kinetics of the sodium storage reaction[36].

The XPS full spectrum reveals the presence of Bi, C, O and N (Fig. S7). In the high-resolution spectrum of Bi 4f, the peaks of Bi $4f_{5/2}$ and $4f_{7/2}$ are detected at 164.52 and 159.23 eV, respectively, which assign to the metallic phase of Bi. Meanwhile, the peaks at 162.44 and 157.14 eV indicate the existence of Bi—O bond (Fig. S8a)[37]. And the C—O bond in the C 1s spectrum (binding energy (BE) = 288.3 eV) and the Bi—O—C bond in the O 1s spectrum (BE = 530.1 eV) indicate the existence of Bi—O—C bond in the Bi@NC composite (Fig. S8b and 8c)[38]. The high-resolution spectrum of N 1s shows the main nitrogen groups including pyridine-N (N-6 at (BE) of 398.31 eV), pyrrole-N (N-5 at BE = 399.34 eV), graphitic-N (N—Q at BE = 400.07 eV), and oxidized-N (N—X at BE = 402.71 eV) (Fig. S8d). Raman spectrum exhibits a prominent peak at 306 cm^{-1} corresponding to Bi—O bonding, indicating the interactions among Bi, O and C elements. These interactions likely contribute to the stabilization of Bi nanoparticles with carbon matrix (Fig. S9)[39]. The peaks observed at 1350 and 1576 cm^{-1} correspond to the *D* and *G* bands, respectively. The calculated intensity ratio (I_D/I_G) of 2.81 suggests a significant presence of defects and active sites within the amorphous carbon layer, attributing to the incorporation of nitrogen atoms. These defects and active sites may be conducive to the Na^+ adsorption and storage[40–41]. Thermogravimetric analysis (TGA) was utilized to determine the bismuth content within the material (Fig. S10). The Bi content in Bi@NC is calculated to be 79.9%, indicating that the proportion of inactive substances in the composite is relatively low.

A 2023 type coin cell has been assembled to examine the Na^+ charge storage characteristics of the Bi@NC composite. The initial CV curve displays several sharp cathodic peaks around 0.45, 0.67, 0.20 and 0.70 V. The emergence of the initial two cathodic peaks corresponds to the alloying reactions. These anodic peaks are preserved and exhibit increased intensity in the following cycle, demonstrating that the Bi@NC material possesses a substantial extent of chemical reversibility. The emergence of the latter two cathodic peaks is likely associated with side reactions occurring between the carbon matrix and the electrolyte. These side reactions result in the forma-

tion of the solid electrolyte interphase (SEI)[42]. However, in the subsequent cycle, the SEI gradually forms and stabilizes, providing a transport channel for ions, resulting in the disappearance of its corresponding reduction peak. Likewise, the two oxidation peaks observed at 0.61 and 0.78 V are indicative of the material undergoing a two-step dealloying process (Fig. 2a and Fig. S11a)[27]. Fig. S11b summarizes the typical GCD curves of this composite anode at 0.5 A g^{-1}. It can be similarly observed that the discharging curves show the clear plateaus at ~ 0.67 and ~ 0.45 V, corresponding to the alloy reactions of Bi → NaBi → Na_3Bi, whereas the plateaus of the charging curves at ~ 0.59 and ~ 0.75 V correspond to the de-alloying reactions at the anode electrode, and this finding is in align with the results obtained from the CV curves.[43]. Furthermore, the initial Coulombic efficiency (CE) of the half-cell was determined to be approximately 52%, indicating that there is a large amount of active sodium loss in 1st cycle. This phenomenon primarily is attributed to the formation of SEI for isolating electrons and transporting ions in the first cycle, and the carbon matrix catalyzes the electrolyte decomposition, resulting in a loss of capacity[44]. Nonetheless, in subsequent cycles, the cell's CE remains consistently above 99% and the GCD curves tend to overlap, which indicate that Bi@NC is highly reversible and with good cycling stability. As the current density increases to 40 A g^{-1}, the specific capacity stabilizes at 300 mAh g^{-1}. Even when the current density is increased to 75 A g^{-1}, the specific capacity of 120 mAh g^{-1} still can be maintained (Fig. 2b) and the voltage plateaus of the cell are still present, indicating that the polarizability of the material is very low (Fig. 2c). In contrast, the rate performance of Bi@NC achieved at 900 °C is apparently higher than that of Bi@NC samples achieved at 800 and 1000 °C (Fig. S12).

To preliminarily verify the potential of Bi@NC to achieve kinetic matching of the anode and cathode

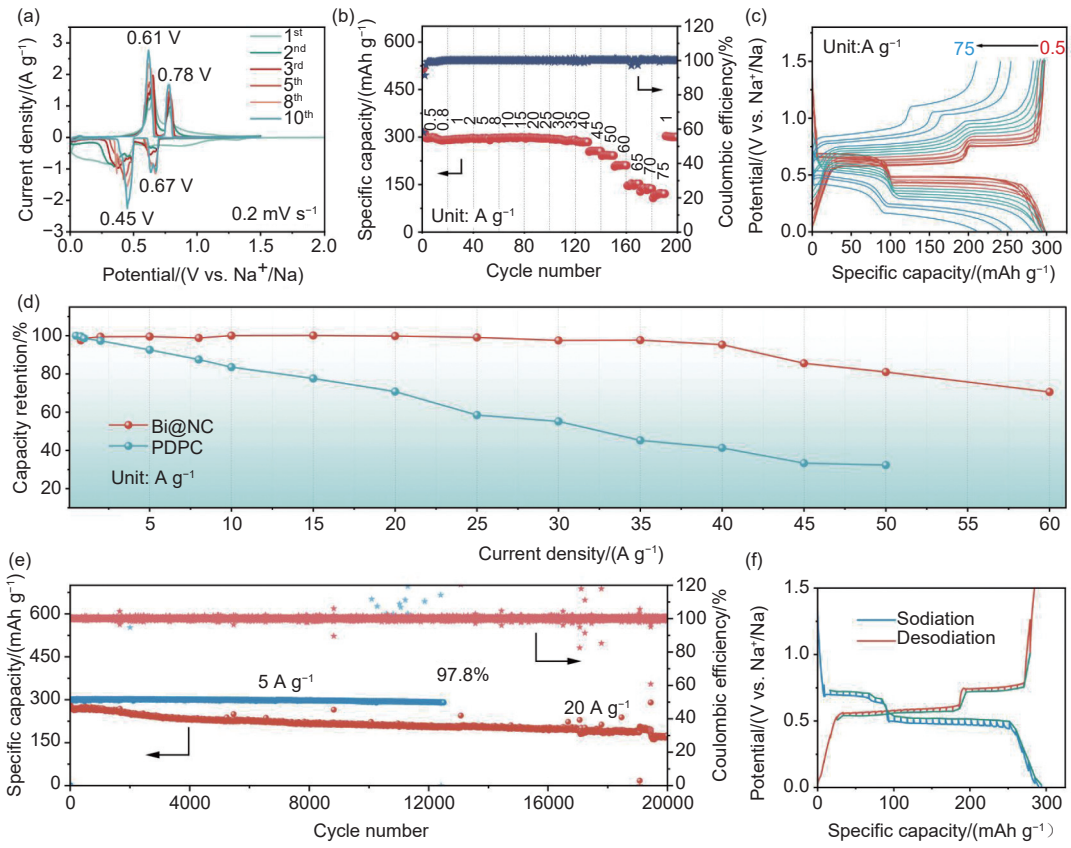

Fig. 2 Electrochemical performance of the Bi@NC composite. (a) CV curves at the previous cycles. (b) Rate performance. (c) GCD curves at different current densities. (d) Rate capability and comparison with PDPC cathode. (e) Cycling performance at 5.0 and 20 A g^{-1}. (f) GITT curves from GITT at 0.1 A g^{-1}

in SICs, the rate performance was compared with homemade PDPC. The GCD curve, rate and cycling results of PDPC are summarized in Fig. S13. PDPC exhibits a specific capacity of 98.3 mAh g^{-1} and maintains at 30.5 mAh g^{-1} under 50 A g^{-1}, suggesting its high-rate capability. Furthermore, PDPC can cycle more than 10 000 cycles with a capacity retention rate of 94% at 5 A g^{-1}, indicating the excellent cycling performance of PDPC. More importantly, Fig. 2d shows that the capacity retention rates of Bi@NC and PDPC are almost the same as the current density is less than 2.0 A g^{-1}. Nevertheless, at 5 A g^{-1}, the capacity retention of Bi@NC remains above 99%, while that of PDPC decreases to 92.58%. When the current density exceeds 15 A g^{-1}, the capacity retention of PDPC decreases to less than 80%, while that of Bi@NC remains almost unchanged, indicating that Bi@NC has better rate performance than PDPC and has the potential to achieve the kinetic matching. Furthermore, this composite electrode demonstrates exceptional cycling stability, with a capacity retention of 97.8% after 12 000 cycles at 5 A g^{-1}. Upon a cycling current of 20 A g^{-1}, a capacity retention rate of 70% is achieved after 17 000 cycles, while the CE is consistently maintained at approximately 100% (Fig. 2e). The cycle stability and rate performance of Bi@NC have significant advantages compared with other similar materials reported so far (Table S1).

To conduct a more in-depth investigation into the reaction kinetics of Bi@NC, the *b* value was calculated by $i=av^b$ from CV curves. According to previous literature reports, when the *b* value is close to 0.5, it indicates that the reaction process is controlled by diffusion. When the *b* value is close to 1, the reaction process is mainly controlled by surface capacitance[45]. At the scan rates of 0.2–10 mV s^{-1}, the *b* value is 0.7–0.8 (Fig. S14a), which suggests that the charge storage process is a hybrid process based on surface capacitance process and diffusion-controlled battery behavior. The appearance of surface capacitive energy storage behavior can be attributed by the presence of Bi nanoparticles and mesoporous structures, which help to shorten the Na^+ transport path, thereby accelerating the transport of Na^+ in Bi@NC composites and promoting the formation of surface control behavior. And as the scan rate is above 10 mV s^{-1}, the *b* value decreases to about 0.5 (Fig. S14b), and such phenomena are consistent with previous results in the literatures[46–47]. It shows that the charge storage process gradually shifts from surface capacitance control to diffusion control at higher scanning rates. This transition may be due to that the kinetics of the electrode reaction is limited by the diffusion rate under fast scanning conditions[48–49].

The GITT was employed to further examine the diffusion kinetics of Na^+ in Bi@NC. The green line in Fig. 2f indicates the quasi-equilibrium voltage, and the overpotentials associated with both the sodiation and desodiation processes are minimal, compared to the initial potentials (<0.1 V), which suggests that the rapid diffusion kinetics of Na^+ in the Bi@NC composites[38]. To further validate the rapid kinetics and structural stability of Bi@NC, EIS was utilized. The progression of impedance can be primarily categorized into two distinct regions: a semicircular feature observed in the mid-to-high frequency range and a linear segment present in the low frequency range, which correspond to the interface impedance (R1) and the charge transfer impedance (R2) of Bi@NC, respectively (Fig. S15a and S15b)[50]. After a long cycle, the R2 of the material only increases slightly, which is mainly due to the SEI. R1 does not change significantly, indicating that the ion exchange between the electrolyte and the material interface still has good diffusion kinetics and structural stability.

To exclude the influence of metastable state and detect the phase transition of Bi@NC in real time, in-situ XRD analysis method was used. Fig. 3a and 3b show the in-situ XRD results under initial cycle. Before discharge, the peaks of hexagonal phase Bi (012) and (110) can be detected. With discharge to 0.55 V, the peaks of (012) can be observed to gradually enlarge in intensity and the peaks of tetragonal phase NaBi alloys (100) and (101) appear at around 25.5° and 31.5°. Upon further discharging to 0.38 V, a reduction in the intensity of the NaBi peaks is observed,

and the peaks of the hexagonal phase Na_3Bi located at 20.9° and 32.8° are gradually enhanced until NaBi is completely converted to Na_3Bi. During the next charging process, the diffraction peaks of Na_3Bi are gradually weakened, and the diffraction peaks of NaBi gradually appear. When charged to 0.66 V, Na_3Bi is completely transformed into NaBi. When the charge continues to 1.15 V, the diffraction peaks of NaBi also disappear one after another, replaced by the diffraction peaks represented by the Bi (012) plane. The diffraction peaks of Bi are almost unchanged compared with that before, indicating the reversible sodium storage process of Bi@NC. Ex-situ TEM analyses of the Bi@NC electrode at various stages of sodiation and desodiation were conducted to further elucidate the structural evolution. At 0.01 V, the Bi@NC composites preserve an intact carbon framework structure, as illustrated in Fig. S16a. Fast Fourier Transform (FFT) and Inverse Fast Fourier Transform (IFFT) analyses were conducted on the microregions to determine the lattice spacing of 0.42 nm, corresponding to the (101) crystallographic plane of Na_3Bi (Fig. 3c and 3d). When charged to 1.50 V, that is, after complete desodiation, the structure of Bi@NC composite also remains stable (Fig. S16b). HRTEM and IFFT analyses reveal the presence of metallic bismuth, as illustrated in Fig. 3e and 3f, which is consistent with the findings from the XRD measurements. Building upon the aforementioned results, the sodium ion charge storage mechanism for Bi@NC is schematically summarized in Fig. 3g, which includes 2-step alloy reactions: $Na^+ + Bi + e^- \leftrightarrow NaBi$ and $2Na^+ + NaBi + 2e^- \leftrightarrow Na_3Bi$.

We have further studied the reasons behind the extraordinary rate performance of Bi@NC composites. Like previous studies[30], Bi@NC also experiences a change from bulk into nanoporous structure

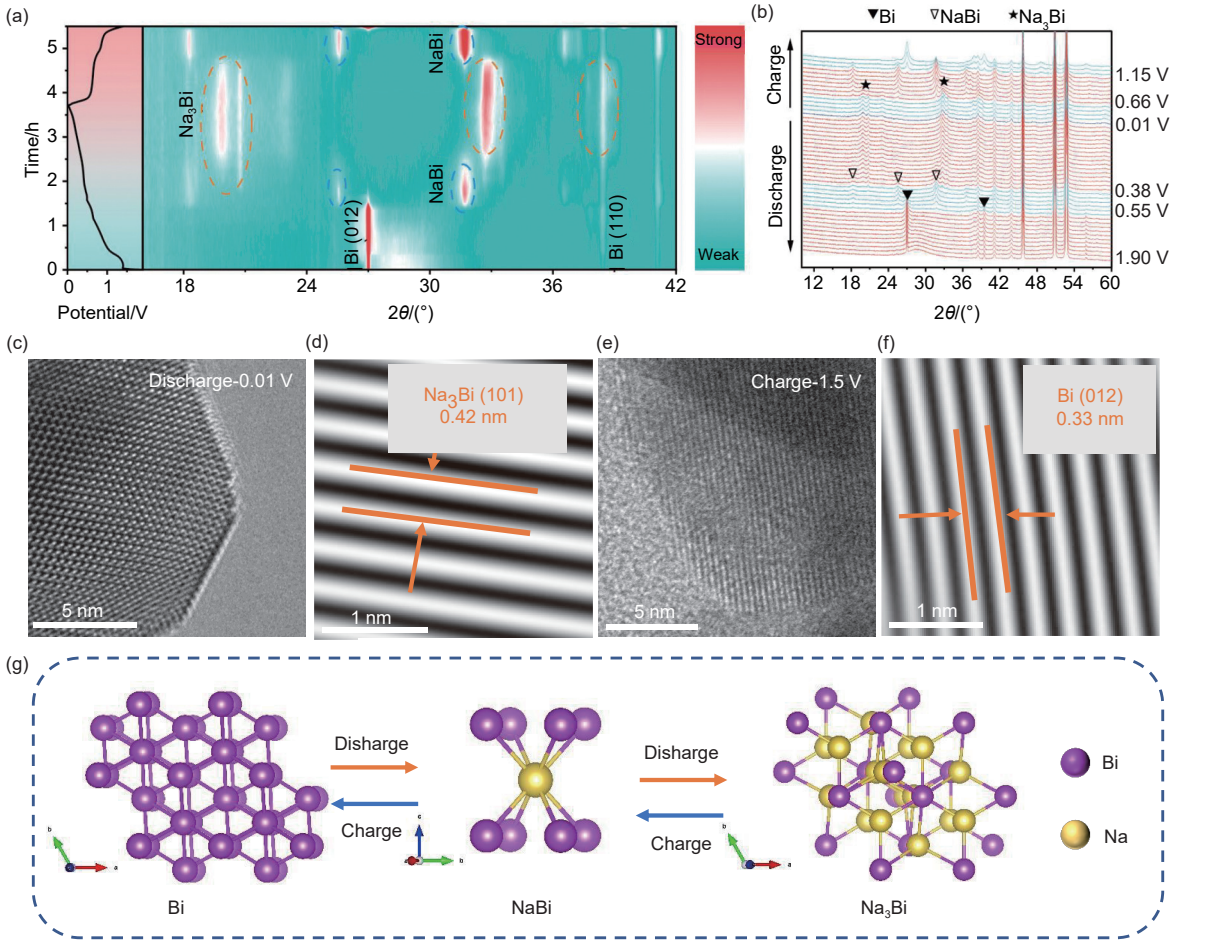

Fig. 3 Structural evolution of Bi@NC. (a, b) In-situ XRD patterns and the corresponding initial (dis-)charge profiles. (c-f) HRTEM images and IFFT images of Bi@NC electrode at different states for the first cycle: (c, d) discharge to 0.01 V, (e, f) charge to 1.50 V. (g) Schematic diagram of alloy phase transition

upon further cycling, as shown in Fig. S17. This is due to the low adsorption tendency of ether-type solvent molecules to bismuth metals, which increases the opportunity for bismuth metals to bind to each other[31]. After the first cycle, the SEI layer is formed, and its morphology has also undergone a preliminary change (Fig. S17a and 17b). As the number of cycles increases, the surface particles gradually aggregate, and a three-dimensional (3D) network structure is formed preliminary after 10 cycles. In the subsequent process, the electrode structure completely evolves into a stable 3D network structure (Fig. S17c and 17d)[26]. This structure can alleviate mechanical stress and decrease surface energy, thereby accommodating volumetric changes during charge and discharge processes and ensuring stable cycling performance. HRTEM analysis reveals that, following 300 cycles, the electrode preserves the three-dimensional network architecture initially identified through SEM (Fig. S18a). It is worth noting that HRTEM image reveals that the carbon frame remains intact and undamaged during charging and discharging, indicating that the resulting stress and strain are effectively alleviated (Fig. S18b). Within the crystalline region, the interplanar spacing measures 0.33 nm, corresponding to the (012) crystallographic plane of bismuth (Fig. S18c). EDS further confirms the integrity of the carbon framework and shows that the metal Bi has formed a stable 3D network structure (Fig. S18d-h). The aforementioned findings and observed phenomena elucidate that the evolution of this structure is the key to the excellent cycle/rate performance of Bi@NC anode materials. Since this structure is formed in repeating alloying/dealloying processes, its local volume expansion stress can propagate around and eventually offset with the volume stress of other parts, thereby eliminating the damage to the carbon skeleton, showing extremely high structural stability and long cycle life. At the same time, this nanoporous structure provides short and abundant ion transport paths, which is conducive to the rapid entry and reaction of sodium ions, showing high ionic conductivity. Moreover, the amorphous carbon skeleton can also provide a high-speed isotropic electron fast transmission network. The high ionic/electronic conductivity endows Bi@NC with unparalleled rate performance.

To prove that Bi@NC is an excellent anode electrode material that can achieve kinetics matching of the anode and cathode in SICs, we used it as an anode and assembled it with self-made PDPC as a cathode into a hybrid capacitor, namely Bi@NC//PDPC (Fig. 4a). During the evaluation of the electrochemical performance of the SIC, the electrochemical window was constrained to a range of 1.0 to 3.5 V. This limitation was primarily implemented to prevent the deposition of sodium metal and the decomposition of the electrolyte, phenomena that typically occur under a broader voltage range. Fig. 4b presents the CV curve of Bi@NC//PDPC SIC at various scan rates from 5 to 200 mV s^{-1}. The CV curve shape of this SIC is different from the traditional ideal capacitor, which is due to the fact that the cathodic and anodic materials of the SIC store Na^+ through different mechanisms (capacitive vs. battery type). The GCD profile exhibits a quasi-triangular shape (Fig. 4c), which indicates that this hybrid cell has good capacitance characteristics. The rate performance evaluation demonstrates that this hybrid cell delivers 51.2 mAh g^{-1} at 0.1 A g^{-1} and 48.2 mAh g^{-1} at 1 A g^{-1}. Notably, at 20 A g^{-1}, this SIC sustains a specific capacity of 32.1 mAh g^{-1}, corresponding to 62.7% of the initial capacity (Fig. 4d). When the current density is back to 1 A g^{-1}, the specific capacity of SIC is back to 48.2 mAh g^{-1}, which is equivalent to nearly 100% reversible specific capacity. The results show that Bi@NC//PDPC possesses remarkable rate performance. The cycle test under different current densities shows that the Bi@NC//PDPC capacitor also exhibits excellent cycle stability (Fig. 4f and 4g). After 3000 cycles at a current density of 0.5 A g^{-1}, SIC can still maintain an initial capacity of 85.9%. When the current density is increased tenfold to 5 A g^{-1}, this hybrid cell can be reversible cycled more than 10 000 cycles. In this case, a capacity retention rate achieves 69.7%. This hybrid cell gains an energy density of 115 Wh kg^{-1} at a power density of 434 W kg^{-1}. Notably, even at an elevated power dens-

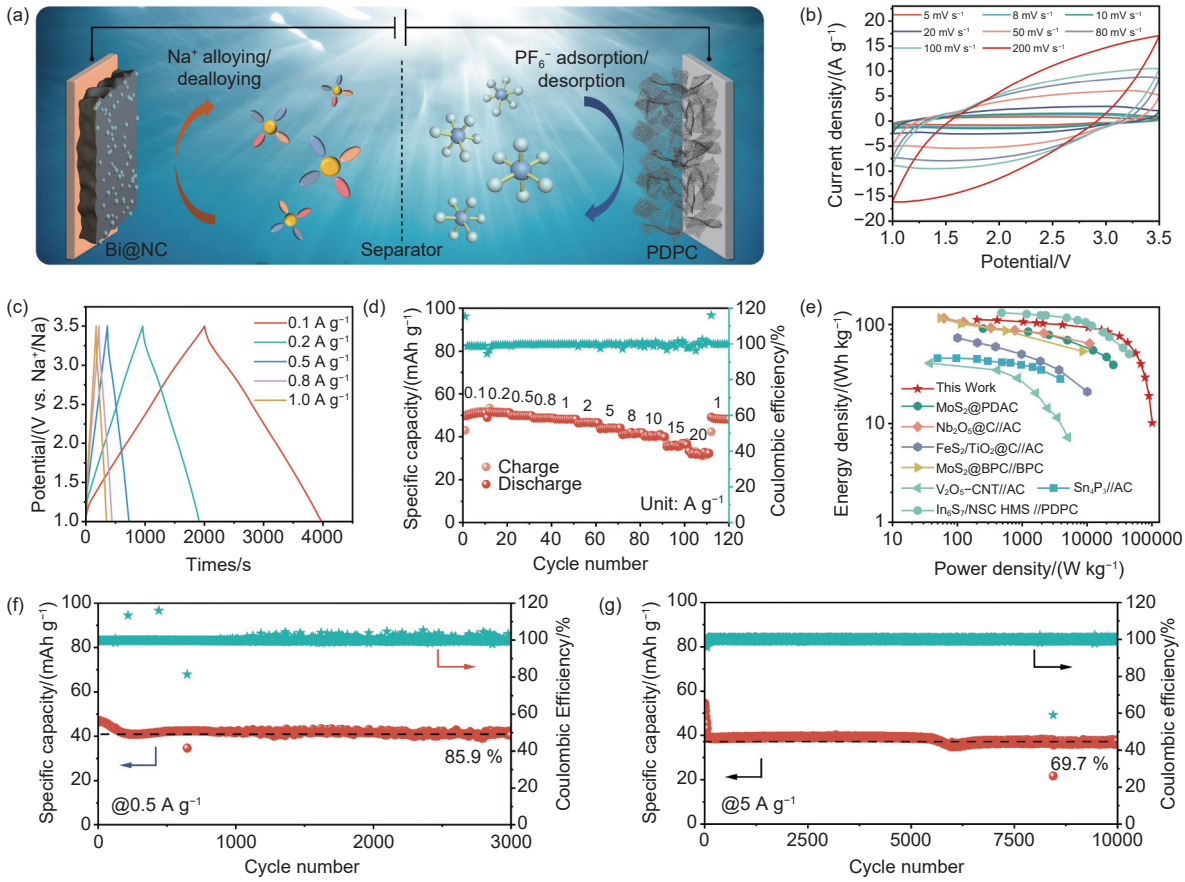

Fig. 4 Electrochemical performance of Bi@NC//PDPC SIC. (a) Schematic image of Bi@NC//PDPC SIC. (b) CV curves. (c) GCD curves. (d) Rate performance. (e) Ragone plots. (f, g) Long-term cycling performance

ity of 45 535 W kg^{-1}, it sustains a substantial energy density of 72 Wh kg^{-1} (Fig. 4e). Compared with the reported capacitors, Bi@NC//PDPC still has considerable energy and power density, such as MoS_2@PDAC//PDPC[51], Nb_2O_5@C//AC[52], FeS_2/TiO_2@C//AC[53], MoS_2@BPC//BPC[54], V_2O_5-CNT//AC[55], Sn_4P_3//AC[56] and In_6S_7/NSC HMS//PDPC[46].

Although the above test results show that Bi@NC has excellent kinetic characteristics, the problem of whether it matches the PDPC cathodic kinetics still needs to be further verified. To this end, we assembled a TESC to dynamically detect the change of the working voltage in the Bi@NC//PDPC capacitor. The structural schematic and circuit diagram of the TESC, which used metallic sodium as the reference electrode, are shown in Fig. S19. We need to further explore the cathode and anode voltage changes to confirm the conjecture. The CV curves of this SIC (expressed in red), and CV curves of the cathode and anode electrodes in the TESC (expressed in blue and green) are shown in Fig. 5a and 5b. At 5 mV s^{-1}, the Bi@NC anode electrode exhibits a voltage range of 0.44 to 0.72 V (vs. Na^+/Na), and the voltage window of the PDPC cathode electrode is 1.72-3.94 V (vs. Na^+/Na). At an elevated scan rate of 50 mV s^{-1}, the CV curve of the Bi@NC//PDPC SICs continues to exhibit a rectangular shape, indicating its good capacitance characteristics. The voltage window of the Bi@NC has been extended to span from 0.33 to 1.00 V, while the voltage window of the PDPC is changed to 2.02–3.84 V. The voltage is in the safe voltage range, and there is no metal deposition and electrolyte decomposition. Additional experiments indicate that as the current density rises (Fig. 5c and 5d), the lower voltage limit of the Bi@NC anode increases from 0.44 to 0.50 V, consistently remaining above the metal deposition potential of 0 V, and the upper limit of the PDPC cathode first increases from 3.93 to 4.00 V, which is always lower than the electrolyte decomposition potential (4.5 V). It is import-

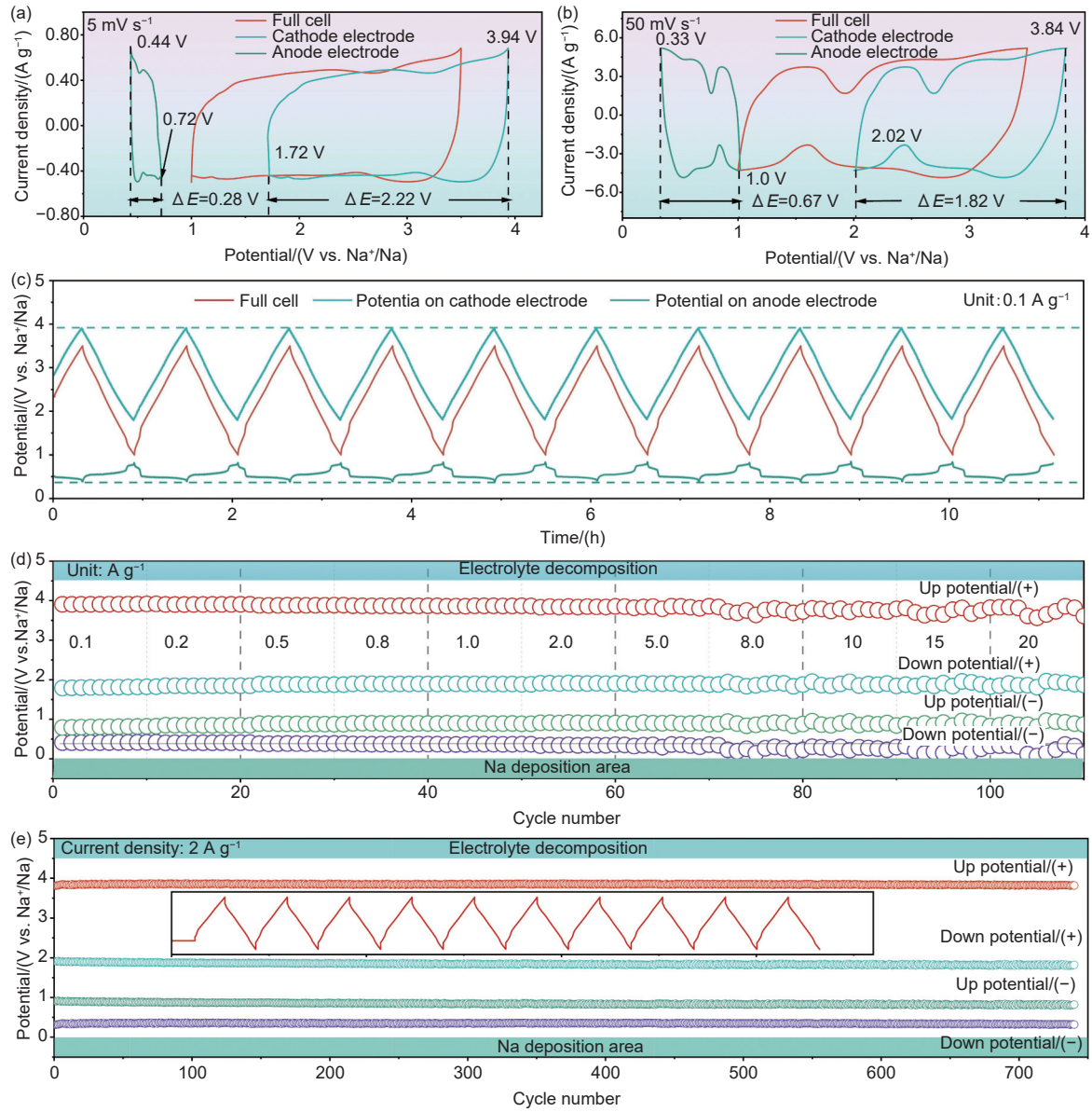

Fig. 5 Kinetics matching assessment between Bi@NC anode and PDPC cathode. (a, b) CV curves of TESC at 5 and 50 mV s^{-1}. (c) The up and down potentials of Bi@NC (−) and PDPC (+) at different charging and discharging rates, and (d) changes in electrode potential windows of Bi@NC (−), PDPC (+). (e) Corresponding upper and lower potentials of Bi@NC (−) and PDPC (+) when cycled at a current density of 2 A g^{-1}

ant to highlight that the voltage window of the anode shifts from 0.43 to 0.46 V, and the voltage window of the PDPC cathode changes from 2.03 to 2.04 V, and both voltage windows remain basically stable.

However, the potential fluctuation of Bi@NC//PDPC capacitor in this study is different from the previous research (such as Graphite//AC LIC). In previous studies, the working potential range of the anode was gradually expanded, while the cathode potential was almost unchanged[57–60]. This kinetic mismatch between the cathode and anode will lead to an expansion of the potential window of the anode observed during high-rate charging and discharging processes to compensate for the capacity attenuation caused by slow kinetics, and sometimes even lead to a decrease in the voltage window of the cathode, thereby reducing the capacity to match the anode. The results show that this work effectively solves the problem of kinetic mismatch between the cathode and anode, and similar rules can be seen in other capacitors[46,51]. In addition, the potential variations of the anode and the PDPC cathode were systematically monitored throughout the extended cycling period. Fig. 5e shows the changes of the cathode and anode

potentials during the long cycle of the SIC. Throughout the entire cycle, the potentials of both the cathode and anode consistently remain within a safe range, which will inhibit the degradation of the electrolyte and the formation of metallic sodium deposits. In addition, the CV curve of SIC remains quasi-triangular throughout the whole process, which further confirms that the Bi@NC//PDPC SIC has good long cycle stability.

4 Conclusion

Bi@NC composites were prepared by a one-step thermal decomposition method using metal Bi salts containing organic ligands as precursors. The carbon framework not only improves the overall conductivity of the material, but also effectively alleviates the stress caused by the volume expansion of the metal Bi during the electrochemical cycle, which is crucial for improving the rate performance and cycle stability of the material. The half-cell evaluation demonstrates that the Bi@NC electrode exhibits excellent rate capability, which is better than AC cathode. Furthermore, a SIC was fabricated by this composite anode, achieving an energy density of 115 Wh kg^{-1} at a power density of 434 W kg^{-1}. At an elevated power density of 45 535 W kg^{-1}, the hybrid device still delivers an energy density of 72 Wh kg^{-1}. The measurements in a TESC confirm that the voltages of both cathode and anode remain within the safe operational range throughout cycling, with minimal voltage variation, thereby indicating robust cycle stability. More importantly, the negligible changes in cathode and anode voltages across different current densities suggest well-matched kinetics between the anode and cathode. This study offers a novel approach for designing SIC anode materials that enable kinetic compatibility between an anode and a cathode.

Acknowledgements

This work was supported by the National Natural Science Foundation of China (52572241, 52272224 and 52402280).

References

[1] Frith J T, Lacey M J, Ulissi U. A non-academic perspective on the future of lithium-based batteries[J]. Nature Communications, 2023, 14(1): 420.

[2] Zhang H, Ishrak M F, Liu X. Development and forecasting of electrochemical energy storage: An evidence from China[J]. Journal of Energy Storage, 2024, 86: 111296.

[3] Waseem M, Lakshmi G S, Ahmad M, et al. Energy storage technology and its impact in electric vehicle: Current progress and future outlook[J]. Next Energy, 2025, 6: 100202.

[4] Zhang Z, Gu Z, Zhang C, et al. Sodium-ion capacitors: Recent development in electrode materials[J]. Batteries & Supercaps, 2021, 4(11): 1680-1700.

[5] Moniruzzaman M, Reddy G R, Ramachandran T, et al. Sodium symphony: Crafting the future of energy storage with sodium-ion capacitors[J]. Journal of Energy Storage, 2024, 95: 112566.

[6] Onoh E U, Khwesa P, Ikhioya I L, et al. Experimental and theoretical investigation of high-performance green-synthesized $NaTiO_2$/AC nanocomposite as high-capacity electrodes for next-generation sodium-ion capacitors[J]. Journal of Materials Science, 2024, 59(40): 19210-19227.

[7] Mysyk R, Carriazo D, Saurel D, et al. The value chain of sustainable dual carbon sodium ion capacitors[J]. Batteries & Supercaps, 2025: e202400807.

[8] Wang L, Hu M, Yao Q, et al. Advanced materials for sodium-ion capacitors: Progress and perspectives[J]. Energy Storage Materials, 2025, 78: 104285.

[9] Ding J, Hu W, Paek E, et al. Review of hybrid ion capacitors: From aqueous to lithium to sodium[J]. Chemical Reviews, 2018, 118(14): 6457-6498.

[10] Tatrari G, An R, Shah F U. Designed metal-organic framework composites for metal-ion batteries and metal-ion capacitors[J]. Coordination Chemistry Reviews, 2024, 512: 215876.

[11] Vanaraj R, Arumugam B, Mayakrishnan G, et al. Advancements in metal-ion capacitors: Bridging energy and power density for next-generation energy storage[J]. Energies, 2025, 18(5): 1253.

[12] Zhai Z, Zhang L, Du T, et al. A review of carbon materials for supercapacitors[J]. Materials & Design, 2022, 221: 111017.

[13] Wu C Y, Chang C Y, Tsai S W, et al. Activated carbon for supercapacitor electrodes produced by the carbonation and activation of glucose with potassium nitrate[J]. ACS Applied Energy Materials, 2024, 7(16): 6873-6886.

[14] Choi J M, Kang Y C, Roh K C. Enhanced supercapacitor stability through irreversible oxygen removal from activated carbon[J]. Journal of Energy Storage, 2025, 110: 115235.

[15] Jaouadi M, Andolsi A, Ghodbane O. Activated carbon–aluminum oxide composite material on nickel foam as supercapacitor electrode in KOH electrolyte[J]. Energy Technology, 2025: 2500123.

[16] Biswal M, Banerjee A, Deo M, et al. From dead leaves to high energy density supercapacitors[J]. Energy & Environmental Science, 2013, 6(4): 1249.

[17] Yan J, Fan Z, Wei T, et al. Fast and reversible surface redox reaction of graphene–MnO_2 composites as supercapacitor electrodes[J]. Carbon, 2010, 48(13): 3825-3833.

[18] Zhang L L, Li H H, Shi Y H, et al. A novel layered sedimentary rocks structure of the oxygen-enriched carbon for ultrahigh-rate-performance supercapacitors[J]. ACS Applied Materials & Interfaces, 2016, 8(6): 4233-4241.

[19] Xia Q, Yang H, Wang M, et al. High energy and high power lithium-ion capacitors based on boron and nitrogen dual-doped 3D carbon nanofibers as both cathode and anode[J]. Advanced Energy Materials, 2017, 7(22): 1701336.

[20] Nagaraju P, Alsalme A, Alswieleh A, et al. Facile in-situ microwave irradiation synthesis of TiO_2/graphene nanocomposite for high-performance supercapacitor applications[J]. Journal of Electroanalytical Chemistry, 2018, 808: 90-100.

[21] Yuan S, Lai Q, Duan X, et al. Carbon-based materials as anode materials for lithium-ion batteries and lithium-ion capacitors: A review[J]. Journal of Energy Storage, 2023, 61: 106716.

[22] Shao Y, Zhang Y, Jiang N, et al. Two-dimensional materials as sodium-ion battery anodes: The mass transfer and storage mechanisms of "fat" Na^+[J]. iScience, 2023, 26(12): 108470.

[23] Pell W G, Conway B E. Peculiarities and requirements of asymmetric capacitor devices based on combination of capacitor and battery-type electrodes[J]. Journal of Power Sources, 2004, 136(2): 334-345.

[24] Man X, Min X, Yan Y, et al. Prospect of bismuth and its compounds in sodium-ion batteries: A review[J]. Energy Storage Materials, 2025, 75: 104076.

[25] Su D, Dou S, Wang G. Bismuth: A new anode for the Na-ion battery[J]. Nano Energy, 2015, 12: 88-95.

[26] Guo S, Wei C, Wang L, et al. Micro-sized porous bulk bismuth caged by carbon for fast charging and ultralong cycling in sodium-ion batteries[J]. Cell Reports Physical Science, 2023, 4(7): 101463.

[27] Lv Z, Xu H, Xu W, et al. Quasi-Topological intercalation mechanism of $Bi_{0.67}NbS_2$ enabling 100 C fast-charging for sodium-ion batteries[J]. Advanced Energy Materials, 2023, 13(25): 2300790.

[28] Park B, Lee S, Han D Y, et al. Multiscale hierarchical design of bismuth-carbon anodes for ultrafast-charging sodium-ion full battery[J]. Applied Surface Science, 2023, 614: 156188.

[29] Wei S, Yang Y, Chen J, et al. A fast-charging and ultra-stable sodium-ion battery anode enabled by N-doped Bi/BiOCl in a carbon framework[J]. Advanced Energy Materials, 2024: 2401825.

[30] Kim Y, An J, Kim S, et al. Enabling 100 C fast-charging bulk bi anodes for Na-ion batteries[J]. Advanced Materials, 2022, 34(27): 2201446.

[31] Kim Y, An J, Li X, et al. Solvent-driven transformation of microsized metal particles into a nanoporous structure and its application to ultrafast-charging batteries[J]. Advanced Functional Materials, 2023, 33(36): 2301552.

[32] Liu Z K, Zhou B, Zhang Y, et al. Discovery of a three-dimensional topological dirac semimetal, Na_3Bi[J]. Science, 2014, 343(6173): 864-867.

[33] Seifert G, Kaschner R, Schöne M, et al. Density functional calculations for Zintl systems: structure, electronic structure and electrical conductivity of liquid NaSn alloys[J]. Journal of Physics: Condensed Matter, 1998, 10(6): 1175-1198.

[34] Zhang E, Wang T, Yu K, et al. Bismuth single atoms resulting from transformation of metal–organic frameworks and their use as electrocatalysts for CO_2 reduction[J]. Journal of the American Chemical Society, 2019, 141(42): 16569-16573.

[35] Liang Y, Song N, Zhang Z, et al. Integrating Bi@C nanospheres in porous hard carbon frameworks for ultrafast sodium storage[J]. Advanced Materials, 2022, 34(28): 2202673.

[36] Cao Y, Wei S, Zhang H, et al. Bismuth nanoparticles embedded in carbon fibers as flexible and free-standing anodes for efficient sodium ion batteries[J]. RSC Advances, 2024, 14(54): 39921-39926.

[37] Zhang Q, Mao J, Pang W K, et al. Boosting the potassium storage performance of alloy-based anode materials via electrolyte salt chemistry[J]. Advanced Energy Materials, 2018, 8(15): 1703288.

[38] Xiong P, Bai P, Li A, et al. Bismuth nanoparticle@carbon composite anodes for ultralong cycle life and high-rate sodium-ion batteries[J]. Advanced Materials, 2019, 31(48): 1904771.

[39] Trentelman K. A note on the characterization of bismuth black by Raman microspectroscopy[J]. Journal of Raman Spectroscopy, 2009, 40(5): 585-589.

[40] Wang T, Tian Z, Hu X, et al. N/P doping-induced defective pore engineering in hard carbon for rapid sodium ion storage and transport[J]. Journal of Power Sources, 2025, 648: 237369.

[41] Min X, Liu J, Chen Y, et al. Mechanically and kinetically reinforced bismuth/carbon microsheets anode for high-power and low-temperature sodium-ion capacitors[J]. Nano Research, 2025, https://doi.org/10.26599/NR.2025.94908219.

[42] Dachraoui W, Pauer R, Battaglia C, et al. Operando electrochemical liquid cell scanning transmission electron microscopy investigation of the growth and evolution of the mosaic solid electrolyte interphase for lithium-ion batteries[J]. ACS Nano, 2023, 17(20): 20434-20444.

[43] Hu C, Zhu Y, Ma G, et al. Sandwich-structured dual carbon modified bismuth nanosphere composites as long-cycle and high-rate anode materials for sodium-ion batteries[J]. Electrochimica Acta, 2021, 365: 137379.

[44] Yang H, Chen L W, He F, et al. Optimizing the void size of yolk–shell Bi@Void@C nanospheres for high-power-density sodium-ion batteries[J]. Nano Letters, 2020, 20(1): 758-767.

[45] Zhang X, Cui X, Yan X, et al. Mechanochemical synthesis of porous graphitic carbon for zinc-ion hybrid capacitors[J]. Electrochimica Acta, 2025, 543: 147582.

[46] Zhu C, Yu W, Zhang S, et al. Hexaindium heptasulfide/nitrogen and sulfur Co-doped carbon hollow microspindles with ultrahigh-rate sodium storage through stable conversion and alloying reactions[J]. Advanced Materials, 2023, 35(16): 2211611.

[47] Shao M, Li C, Li T, et al. Pushing the energy output and cycling lifespan of potassium-ion capacitor to high level through metal–organic framework derived porous carbon microsheets anode[J]. Advanced Functional Materials, 2020, 30(51): 2006561.

[48] Zhang X, Jiang C, Zhao J, et al. Porous and graphitic carbon nanosheets with controllable structure for zinc-ion hybrid capacitor[J]. Journal of Colloid And Interface Science, 2024, 664: 146-155.

[49] Zhang X, Wang R, Li H, et al. Selection and optimization of carbon precursor to prepare porous graphitic carbon for zinc-ion hybrid capacitor[J]. Journal of Energy Storage, 2025, 113: 115741.

[50] Vivier V, Orazem M E. Impedance analysis of electrochemical systems[J]. Chemical Reviews, 2022, 122(12): 11131-11168.

[51] Yu W, Zhu C, Wang R, et al. Ordered macroporous MoS_2-carbon composite with fast and robust sodium storage properties to solve the issue of kinetics mismatch of sodium-ion capacitors[J]. Energy & Environmental Materials, 2023, 6(2): e12337.

[52] Lim E, Jo C, Kim M S, et al. High-Performance sodium-ion hybrid supercapacitor based on Nb_2O_5@carbon core–shell nanoparticles and reduced graphene oxide nanocomposites[J]. Advanced Functional Materials, 2016, 26(21): 3711-3719.

[53] Xiao X, Duan X, Song Z, et al. High-Throughput production of cheap mineral-based heterostructures for high power sodium ion capacitors[J]. Advanced Functional Materials, 2022, 32(18): 2110476.

[54] Li Y, Wang H, Huang B, et al. Mo_2C-induced solid-phase synthesis of ultrathin MoS_2 nanosheet arrays on bagasse-derived porous carbon frameworks for high-energy hybrid sodium-ion capacitors[J]. Journal of Materials Chemistry A, 2018, 6(30): 14742-14751.

[55] Chen Z, Augustyn V, Jia X, et al. High-Performance sodium-ion pseudocapacitors based on hierarchically porous nanowire composites[J]. ACS Nano, 2012, 6(5): 4319-4327.

[56] Chojnacka A, Pan X, Jeżowski P, et al. High performance hybrid sodium-ion capacitor with tin phosphide used as battery-type negative electrode[J]. Energy Storage Materials, 2019, 22: 200-206.

[57] Sun X, Zhang X, Liu W, et al. Electrochemical performances and capacity fading behaviors of activated carbon/hard carbon lithium ion capacitor[J]. Electrochimica Acta, 2017, 235: 158-166.

[58] Huang X, Gao J, Qin Y, et al. Revealing the effect of the microstructure on potassium storage behavior in a two-dimensional mesoporous carbon anode[J]. ACS Nano, 2024, 18(32): 21459-21471.

[59] Qin Y, Gao J, Lu J, et al. Uncovering the effect of crystallinity on the pseudocapacitive behavior of Li^+ storage on disordered rock-salt vanadium oxide[J]. ACS Nano, 2025, 19(31): 28933-28944.

[60] Liu X, Guo W, Zhang Z, et al. Wood's Alloy film anode with fast and durable Na^+ storage[J]. Advanced Functional Materials, 2025: e17951.